Supercapacitor electrode based on ternary activated carbon/CuCoO2 hybrid material

Katia Ait Kaci Azzou, Achour Terbouche, Chafia Ait Ramdane-Terbouche, Thierry Bataille, Didier Hauchard, Djillali Mezaoui

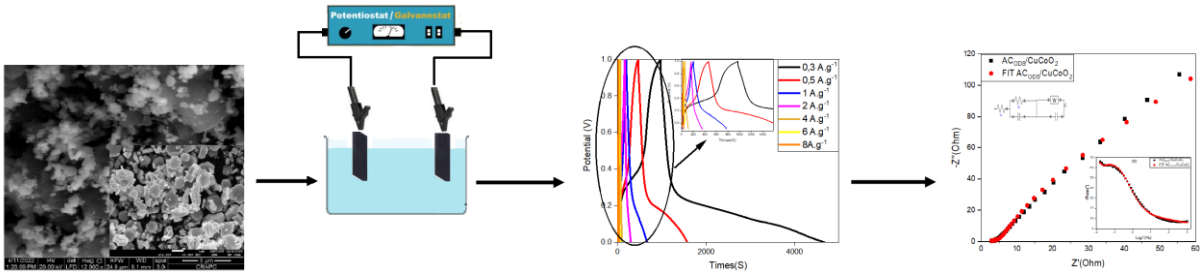

Supercapacitor electrode based on ternary activated carbon/$CuCoO_2$ hybrid material

Katia AIT KACI AZZOU[a,b,c], Achour TERBOUCHE[b,*], Chafia AIT RAMDANE-TERBOUCHE[b], Thiery BATAILLE[c], Didier HAUCHARD[c], Djillali MEZAOUI[a]

[a]Laboratoire Sciences des Matériaux, Faculté de Chimie, Université USTHB, 16111 Alger, Algérie.

[b]Centre de Recherche Scientifique et Technique en Analyses Physico-chimiques (CRAPC), BP384, Bou-Ismail, RP 42004, Tipaza, Algérie.

[c]Université Rennes, ENSC Rennes, CNRS, ISCR-UMR6226, Rennes 35000, France

[*]Corresponding author: achour_t@yahoo.fr ; achour.terbouche@crapc.dz

Tel.: +213.660 37 01 15; Fax: +213.24.325.774

Abstract

In this work, a supercapacitor electrode was prepared using modified ternary activated carbon (AC_{ODS}: Ternary Olive-Date-Sugar activated carbon) by $CuCoO_2$ bimetallic oxide. The hydrothermal synthesis of $CuCoO_2$ was successfully carried out, and then the doping on activated carbon was done. Subsequently, the characterization of the hybrid material by ATR, SEM, XRD, Zeta potential, XPS, Raman, TGA, and electrochemical methods were studied in a binary electrolyte (1M H_2SO_4/KCl). The electrochemical results indicate that $AC_{ODS}/CuCoO_2$ modified electrode exhibits excellent pseudo-capacitive behavior, with a specific capacitance of 1052.95 $F.g^{-1}$ at 0.3 $A.g^{-1}$ and high specific energy (161.23 $Wh.kg^{-1}$) at high current (8 $A.g^{-1}$). High specific capacitance of 103.12 $F.g^{-1}$ and a specific capacitance retention reaches up to 95.41% after 10^4 charge-discharge cycles at 20 $A.g^{-1}$ were also obtained. This study revealed that the activated carbon modified with $CuCoO_2$ oxide offers a significant improvement in the specific capacitance and the specific energy with a high specific current. Based on these results, $AC_{ODS}/CuCoO_2$ can be explored as supercapacitor electrode for energy storage, and that in

terms of specific capacitance, this hybrid material gives the most important result ever obtained with this oxide.

Keywords: Activated carbon-bimetallic oxide, Hybrid material, Supercapacitor electrode, Energy storage.

1. Introduction

Supercapacitors are evolving rapidly due to their unique properties of high-power density, fast charge/discharge and long-term stability [1]. There are two types of supercapacitors; the first one is the electrochemical double-layer supercapacitor (EDLC), mainly based on carbonaceous materials that store charge via absorption and desorption of surface ions at the electrode/electrolyte interface (electrostatic energy). Carbon based materials provide energy in the form of EDLC, which has the lowest specific capacitance and energy specificity [2, 3]. The second one is the pseudo-capacitive supercapacitor that stores charge via fast faradic reactions between ions and electrolyte. This specific capacitance in the pseudo-capacitive is higher than those of EDLC.

Polymers such as polyaniline and polypyrole are used as electrode materials for pseudo-capacitors [4-8]. Several transition metal oxides and hydroxides are also used for the same purpose, including RuO_2, ZrO_2, $NiCo_2O_4$, MnO_2, $MnCo_2O_4$, ZnO, Fe_2O_3, $FeCo_2O_4$, Co_2O_3, and $CuCoO_2$ [9-12]. Due to their various properties, such as high electrical conductivity, wide band gap, high degree of transparency, and high degree of stability [13-19], the binary metal oxides deliver different oxidation states that significantly improve the supercapacitor performance [20]. Among the binary metal oxides, the copper compounds ($CuMO_2$) are used in various applications such as optics [21, 22], magnetism [23, 24], catalysis [25], and as electrode of supercapacitor. In addition, copper-based oxides are low cost and abundant [26, 27]. For our research, we used $CuCoO_2$ that has been studied in various fields, including photocatalysis and

dihydrogen production [28, 29], because it is considered a well-known electrode material due to its excellent morphology and corrosion resistance properties.

The objective of this work is to improve the performance of a ternary activated carbon prepared using olive, date pits and sugar (AC_{ODS}) that we have already studied. In this previous study, we achieved an excellent performance namely a specific capacitance (528 $F.g^{-1}$ at 0.3 $A.g^{-1}$) and high specific energy (36.82 $Wh.kg^{-1}$), however the specific current was low (4 $A.g^{-1}$) [30]. In order to improve the specific current of our AC_{ODS}, we combined it with $CuCoO_2$. In the literature, we could find only very few works using $CuCoO_2$ as one of the cathode active materials with a ratio of 75%, and the results revealed a specific capacitance of 250 $F.g^{-1}$ at 0.5 $A.g^{-1}$ for this material [31].

In this work, high-performance supercapacitor electrodes were prepared using $AC_{ODS}/CuCoO_2$ hybrid material with only 20% of bimetallic oxide. This led to a significant improvement in the electrochemical performance of AC_{ODS}, reaching a record specific current. These very promising results showed that the investigated hybrid material can be used as electrode for low-cost high-performance supercapacitor.

2. Materials and methods

2.1. Apparatus and reagent

ATR spectra were recorded with a BRUKER ALPHA-T spectrometer in the range 4000-400 cm^{-1}. JEOL JSM 7100 F EDS-EBSD Oxford was used for SEM-EDX and cartography analysis. X-ray diffraction (XRD) patterns were recorded on Bruker D8 Advance A25 diffractometer using a Cu K-alpha X-ray source, PSD mode of scanning in 2theta 5-80° range with SSD 160 (mode 1D) and resolution of 2.456°. For identified peaks, ICDD data base was employed. The Zeta potential and hydrodynamic diameter of the colloidal suspensions were measured by a Malvern Nano-ZS Instrument. The X-ray photoelectron spectroscopy (XPS) was carried out

using an ESCALAB 220 XL spectrometer from Vacuum Generators featuring a monochromatic Al Kα X-ray source (1486.69 eV) with a spot size of 250 × 250 µm at an operating power of 180 W. The thermogravimetric study (TGA) was recorded on SDT Q600 thermal analyser under nitrogen atmosphere with a heating rate of 10 °C.mn^{-1} in the range of 0-1000 C°. The electrochemical measurements were performed using the "Nova 2.1" software on a Metrohm Autolab 302N Potentiostat/Galvanostat. All chemical products used to prepare the measuring samples were purchased from Sigma Aldrich or Fluka Chemical Companies, and the aqueous solutions were prepared using free CO_2 deionized water. The mixed aqueous electrolyte (1M H_2SO_4; 98%)/KCl; 99.0-100.5%) was prepared by adding 100 mL of 1M KCl solution to 100 mL of 1M H_2SO_4 solution (1:1 ratio).

2.2. Synthesis of $AC_{ODS}/CuCoO_2$ and electrodes preparation

Synthesis and characterization of AC_{ODS} material and its electrode are reported in our previous study [30]. AC_{ODS} was obtained from crushing a mixture of 5 g date pits, 5 g olive pits and 5 g sugar for 4 h using a planetary mill at 378 rpm. The obtained powder is heated for 1 h at 700 ◦C under an inert nitrogen atmosphere, and the resulting carbon compound was activated using H_3PO_4 (1 M).

$CuCoO_2$ was prepared hydrothermally by mixing 3.6 g of copper(II) nitrate trihydrate ($Cu(NO_3)_2$, $3H_2O$; 99%) and 4g of cobalt(II) nitrate hexahydrate ($Co(NO_3)_2.6H_2O$; 98%) in 60 mL of deionized water at room temperature, then the amount quantity of sodium hydroxide (NaOH/2M; ≥98%) was added until reaching a pH of 12. The mixture was kept under stirring for 2 hours, then the solution was transferred into a 100 mL Teflon-lined autoclave at 100 °C for 24 hours, and a gray solution was recovered and filtered. Finally, the obtained powder was washed several times with distilled water and ethanol, then dried in an oven at 60 °C.

The hybrid $AC_{ODS}/CuCoO_2$ material was synthesized by combining 0.08 g of activated carbon (AC_{ODS}) with 0.02 g $CuCoO_2$ in 10 mL of water (Fig. 1). The mixture is then placed in an ultrasonic bath for agitation for 24 hours. The final product is filtered and dried in an oven at 50°C.

The working electrodes were prepared in two steps: first, 0.1 g of the $AC_{ODS}/CuCoO_2$ compound was placed in 10 mL of water, and ultrasonically treated until a colloidal solution was obtained, then 100 µL of this solution was deposited on the surface of carbon paper (HCP030N; 1 x 2 cm^2). Finally, the resulting electrode was placed in an oven at 50°C for 24 hours.

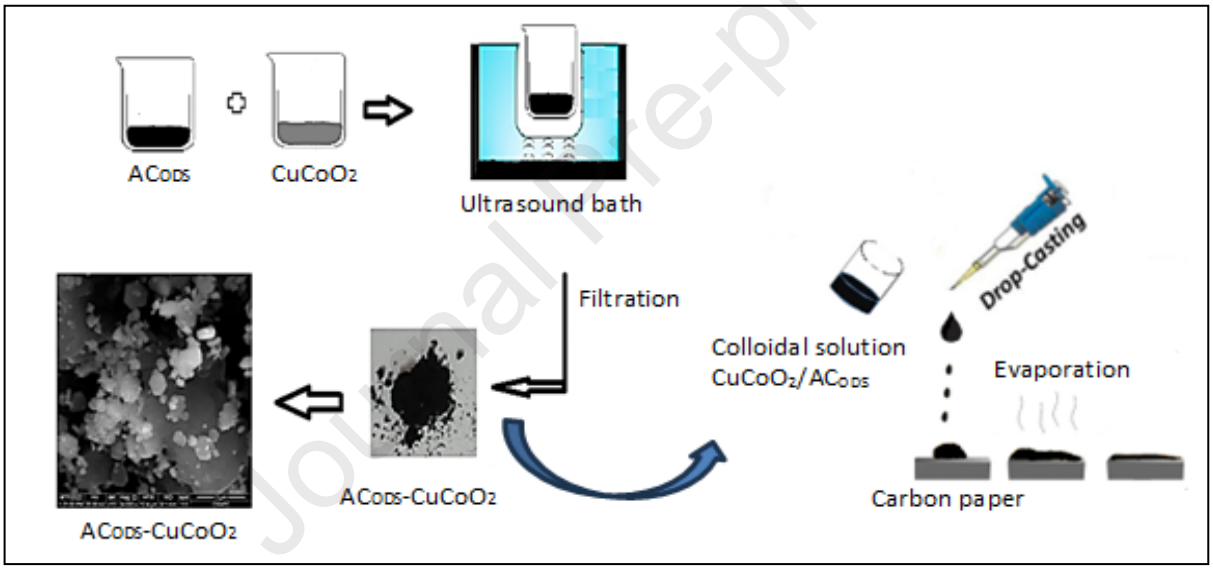

Fig. 1. Synthesis route of $AC_{ODS}/CuCoO_2$ hybrid material and electrode preparation.

The preparation of the two electrode symmetrical systems is performed as follows:

After cutting two sheets of 1x2 cm^2 carbon paper, a colloidal in aqueous solution of the $AC_{ODS}/CuCoO_2$ material is prepared. Using the Droop Casting method, 100 µL of the obtained solution is deposited on a 1cm^2 surface of each previously cut paper, ensuring complete coverage of the surface. After drying for 24 hours, the process is checked to ensure perfect symmetry between the two electrodes. Once the identical electrodes are ready, they are

completely immersed in the electrolyte and well separated from each other in order to carry out the electrochemical studies.

2.3. Electrochemical studies

The electrochemical behavior was studied using a three-electrodes electrochemical cell in a mixture electrolyte (1M H_2SO_4/KCl) using carbon paper, Metrohm Pt wire and Ag/AgCl as working, counter and reference electrodes, respectively. Cyclic voltammetry measurements (CV) were performed from -0.6 and 1 V at different scan rates.

To better understand the charge storage dynamics of the prepared electrode, the b value from the CV spectra is determined using Dunn's power law relationship following the equation below:

$$i = av^b$$

Where *i* obeys a power law relationship with the scan rate *v*; *a* and *b* are adjustable parameters, and *b*-values are calculated from the slope of the plot of *log (i) vs. log (v).*

Galvanostatic charge-discharge (GCD) was performed at different specific currents 0.3, 0.5, 1.0, 2.0, and 4.0 A.g $^{-1}$ with three electrodes, and 0.3, 0.5, 1.0, 2.0, 4.0, 6.0, 8.0, and 10.0 A.g^{-1} with two electrodes. The electrochemical parameters such as specific capacity (Qs/mAh.g^{-1}), specific capacitance (C/F.g^{-1}), specific energy (E/Wh.Kg^{-1}), specific power (P/W.Kg^{-1}), were calculated through the galvanostatic charge-discharge curves.

So, from these curves recorded using two symmetric electrodes, the specific capacitance as well as the specific energy and the specific power have been calculated [32], and the specific capacity has been calculated from three electrodes according to the following equations (1) and (2) [33, 34]:

$$C = \frac{I \times \Delta t}{\Delta V \times m} \text{ ……..(1)}$$

$$\text{Qs} = \frac{Id \times \Delta t}{3.6} \text{ ……(2)}$$

Where I is the discharge current (A), Δt is the discharge time (s), ΔV is the voltage variation (V), and m is the mass of the active material (g). For specific capacity: Id is specific currents ($A.g^{-1}$). The specific energy and specific power of a supercapacitor were determined using the following Eqs. (3) and (4) [35, 36]:

$$E(Wh.kg^{-1}) = \frac{C}{7.2}(\Delta V)^2 \ldots\ldots (3)$$

$$P(W.kg^{-1}) = \frac{3600 \times E}{\Delta t} \ldots\ldots\ldots (4)$$

The cycling stability was evaluated using the galvanostatic charge-discharge method at 20 $A.g^{-1}$ for 10^4 cycles. Finally, The electrochemical impedance spectroscopy (EIS) was studied in the frequency range from 100 kHz to 10 mHz with a sinusoidal signal amplitude of 10 mV.

3. Results and discussion

3.1. Attenuated total reflectance spectroscopy (ATR)

Comparing the ATR spectra of $CuCoO_2$ and $AC_{ODS}/CuCoO_2$ revealed the disappearance, reappearance, and displacement of several vibrational bands associated with various functional groups. The ATR spectrum of $CuCoO_2$ in the 4000-400 cm^{-1} wavenumber region, as shown in Fig. 2a, exhibits two main absorption peaks at approximately 550 and 750 cm^{-1}, which are attributed to the vibration of Cu-O and Co-O bonds, respectively [37, 38]. In the ATR spectrum of $CuCoO_2$, the broad band located in the 3400-1200 cm^{-1} region combines the stretching vibration of the C-O bonds due to CO_2 and the O-H bonds due to moisture absorbed in the atmosphere (hydrating water molecules) [39].

In the ATR spectrum of $AC_{ODS}/CuCoO_2$ hybrid material (Fig. 2b), the vibration peaks of Cu-O and Co-O were shifted to lower wavenumbers and their intensities are decreasing. This is due to the interaction between the activated carbon surface and the bimetallic oxide, and the decrease in the quantity of $CuCoO_2$ in the mixture [40]. The bands around 2900, 2800 and 1530 cm^{-1} can be attributed to the stretching vibrations of CH, CH_2 and C=C groups of activated

carbon. Some peaks were shifted to higher and lower wavenumbers, indicating potential chemical interactions between the activated carbon surface and bimetallic oxide. In addition, this chemical interaction leads to a decrease in the intensity of the Cu-O and Co-O band vibration. The OH band exhibits low intensity in this spectrum, which is probably due to the interaction between the activated carbon and $CuCoO_2$ via the hydroxyl and carboxyl functional groups [41]. These results indicate the successful incorporation of $CuCoO_2$ into the activated carbon matrix.

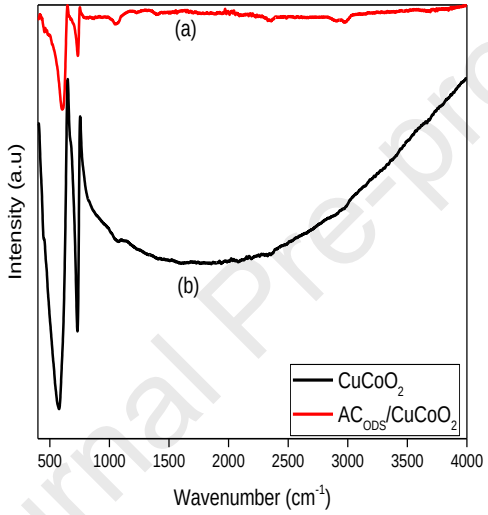

Fig. 2. ATR spectra: (a) $AC_{ODS}/CuCoO_2$ and (b) $CuCoO_2$.

3.2. Scanning electron microscopy- Energy-dispersive X-ray spectroscopy (SEM-EDX)

SEM micrographs of the $CuCoO_2$ oxide surface are reported in figure S1. The delafossite feature of the hexagonal structure can be clearly seen. The micrographs show well-defined hexagonal crystals that appear more and more well-structured with increasing magnification. The latter crystals are particles of size 1µm in diameter and 100 nm in thickness, which confirm the hexagonal structure of the prepared oxide obtained by XRD.

To analyze the chemical composition of $CuCoO_2$, SEM-EDX mapping was studied. Fig. S2 shows typical areas selected (1-4) for EDX analysis. The spectra of $CuCoO_2$ indicate that the

sample contains Co, Cu and O elements. The quantitative analysis shows that the weight of the three elements are respectively, copper around 25%, cobalt around 22% and oxygen around 51%. Hence, this result confirm the good formation of the $CuCoO_2$ oxide.

Fig. S3 shows the elemental mapping analysis of prepared $CuCoO_2$ oxide and the images revealed that an uniform distribution of copper (Cu), cobalt (Co) and oxygen (O) has observed in the picked region of the oxide.

SEM micrographs recorded with the activated carbon/oxide hybrid material ($AC_{ODS}/CuCoO_2$) (Fig. 3), revealed the formation of the desired hybrid material ($AC_{ODS}/CuCoO_2$) and the penetration of the oxide particles ($CuCoO_2$) into the pores of the activated carbon (AC_{ODS}). This observation is demonstrated by comparing the SEM images of the AC_{ODS} before (Fig. 3a) and after $CuCoO_2$ deposition (Fig. 3b-d). It should be noted that before deposition, the pores are empty.

The deposition of the oxide on the activated carbon has also been demonstrated using other characterizations such as XPS, Raman and TGA, which are studied below.

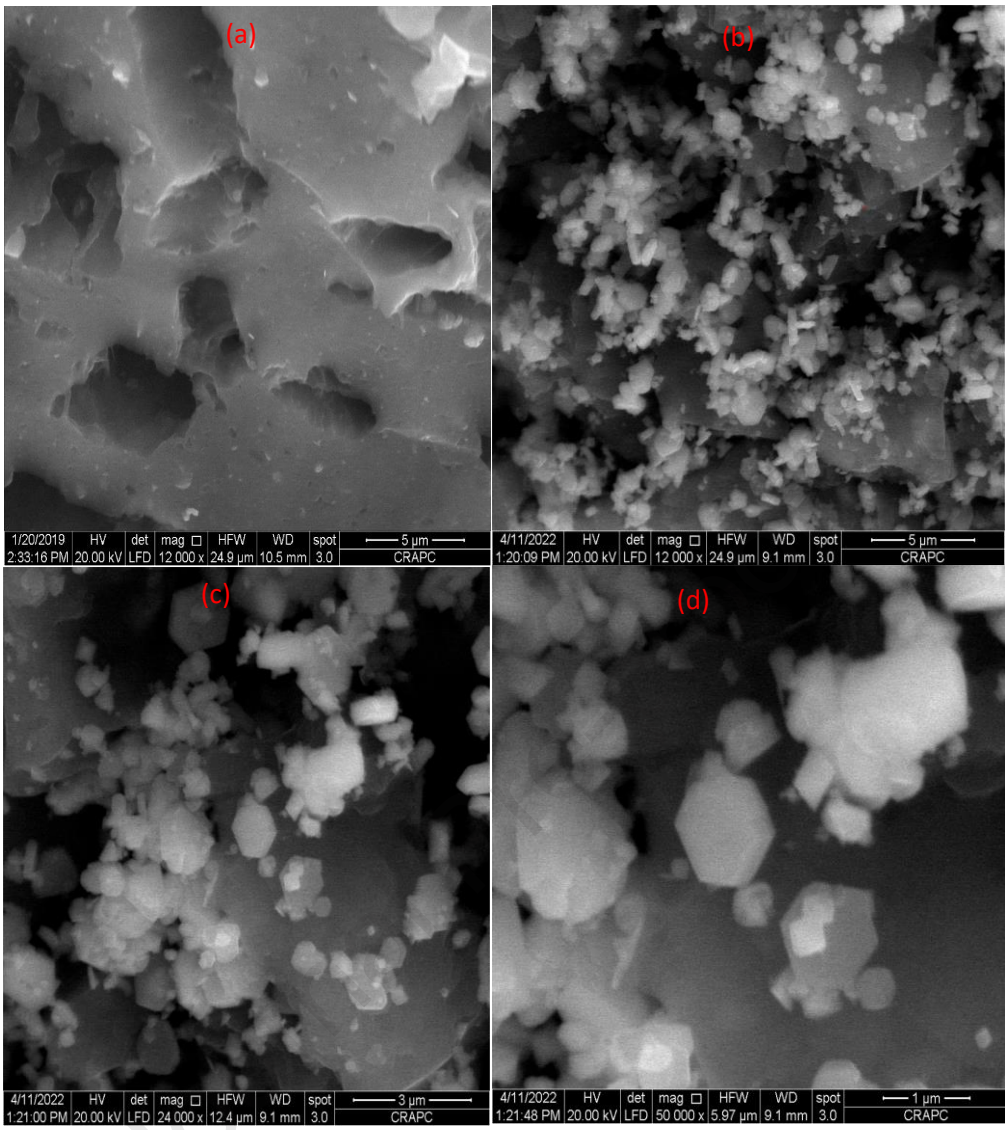

Fig. 3. SEM micrographs of (a) AC_{ODS} [30] and (b-d) $AC_{ODS}/CuCoO_2$ hybrid material (5, 3 and 1µm).

3.4. X-ray diffraction

The synthesized products ($CuCoO_2$ and $AC_{ODS}/CuCoO_2$) were analyzed by X-ray diffraction and their diffractograms are shown in Fig. 4. According to the crystallographic data base ICSD N 00-021-0256, the spectrum in Fig. 4a demonstrates the presence of quasi homogeneous phase. The structure is fine-tuned in the R-3m space group. All peaks are indexed in the hexagonal system with a=b=2.85 A° and c=16.82 A° mesh parameters. The characteristic diffraction peaks of $CuCoO_2$ are located at 15.7°, 31.7°, 37.7°, 39.6°, 43.62°, 44.4°, 57.2°, 61.8°, 65.1°, 66.9°,

and 74.2°. It is worth noting that we have obtained an almost pure phase of $CuCoO_2$ for the first time using a low-temperature hydrothermal method (100 °C), which has several advantages over the high-temperature hydrothermal reaction, which inherently generates impurities. In contrast, Fig. 4b shows that the diffractogram of the $AC_{ODS}/CuCoO_2$ hybrid compound displays peaks similar to those of the oxide alone with a pattern that reflects the presence of the carbonaceous material in the activated carbon (AC_{ODS}).

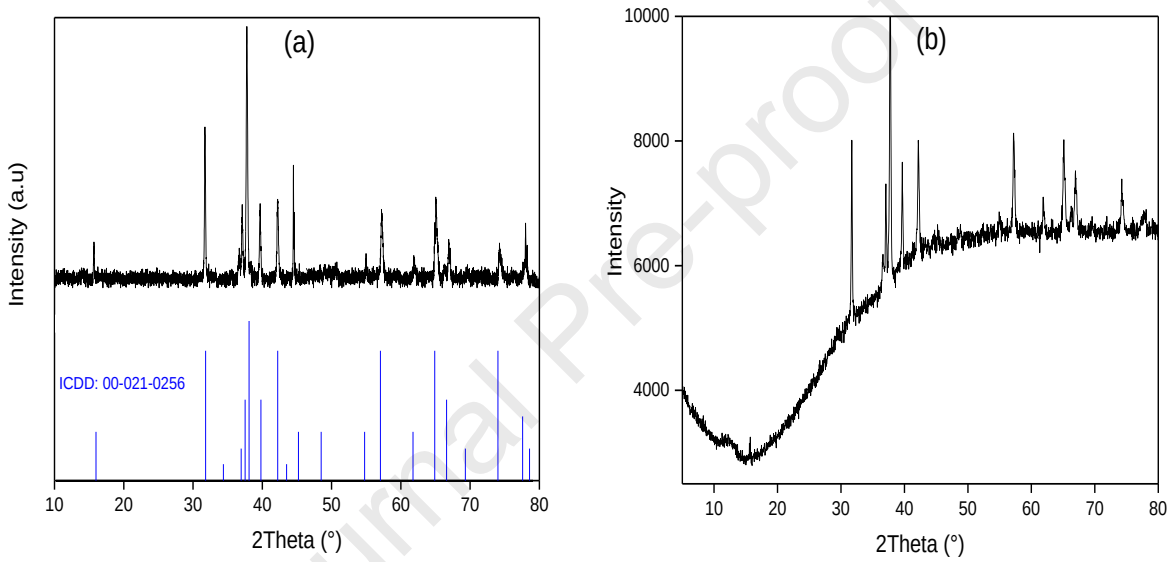

Fig. 4. X-ray diffractograms of (a) $CuCoO_2$ and (b) $AC_{ODS}/CuCoO_2$ hybrid material.

3.5. Zeta potential and particle size distribution

The Zeta potential (Fig. 5a, b) and the size (Fig. 5c, d) of $CuCoO_2$ and $AC_{ODS}/CuCoO_2$ were measured to study the charges on the surface. Note that the Zeta potential value indicates that both samples have a negatively charged surface [42]. The Zeta potential of the oxide is -30.2 mV. After the AC_{ODS} modification step, the Zeta potential becomes -43.1 mV, indicating the presence of the negatively charged active carbon groups. This improves the stability of the colloidal solution of the $AC_{ODS}/CuCoO_2$ mixture [43].

As shown in Fig. 5, the particle size of $CuCoO_2$ is 1011.4 nm (Fig. 5c) and $AC_{ODS}/CuCoO_2$ is around 973.7 nm (Fig. 5d). This result indicated that the presence of AC_{ODS} activated carbon reduced the size of oxide particles, which is beneficial for a variety of applications.

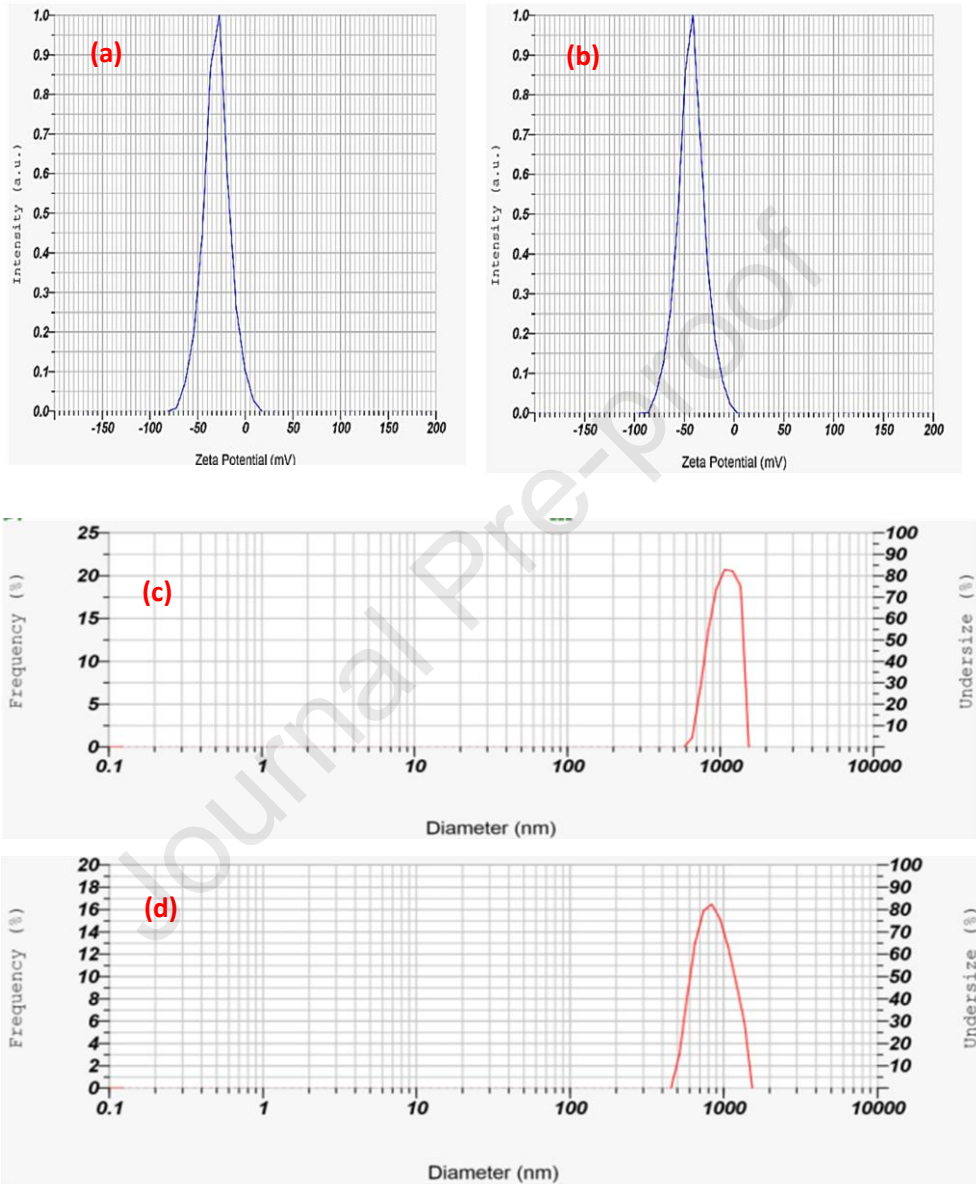

Fig. 5. Zeta potential: (a) $CuCoO_2$; (b) $AC_{ODS}/CuCoO_2$ and Particle size: (c) $CuCoO_2$; (d) $AC_{ODS}/CuCoO_2$.

3.6. XPS Analysis

The X-ray photoelectron (XPS) spectroscopy was carried out to study the chemical composition of the AC_{ODS} and $AC_{ODS}/CuCoO_2$ composite. The binding energy of the different elements was determined from XPS spectra (Fig. 6).

The XPS survey spectrum of AC_{ODS} (Fig. 6a) exhibits two peaks at 287.34 eV (C1s) and 534.17 eV (O1s), respectively, indicating carbon (C) and oxygen (O) as main elements in prepared activated carbon. XPS survey spectrum of $AC_{ODS}/CuCoO_2$ composite recorded in figure 6b showed the presence of peaks localized around 290, 538, 788, and 939 eV, attributed to C1s, O1s, Cu2p, and Co2p elements, respectively. These results confirm the presence of Cu, Co and O in the $AC_{ODS}/CuCoO_2$ material. The peaks of Cu at 939.37 and 958.60 eV correspond to the binding energies of $Cu^+ 2p_{3/2}$ and $Cu^+ 2p_{1/2}$, indicating the presence of monovalent copper cation (Cu^+) in $CuCoO_2$ [44, 45].

In the high-resolution spectra of AC_{ODS}, the C 1s peaks (Fig. 6c) corresponding to C-C, C-O and C=O bonds were observed at 286.16, 286.75 and 287.59 eV, respectively. In addition, the O 1s peaks (Fig. 6d) assigned to C-O and C=O bonds were localized at 533.41 and 534.65 eV, respectively. For $AC_{ODS}/CuCoO_2$ fitting, the C 1s peaks (Fig. 6e) attributed to C-C was shifted to be located around 290 eV, a result already recorded in previous work [46, 47].

The O 1s peaks assigned to the C-O and C=O bonds in $AC_{ODS}/CuCoO_2$ were detected at 537.16 and 538.80 eV (Fig. 6f).

The XPS spectrum recorded for Co element is reported in Fig. 6g. The main peaks corresponding to electronic levels Co $2p_{3/2}$ and Co $2p_{1/2}$ are associated to two shake-up satellites [48]. For the high-resolution spectrum of Cu2p (Fig. 6h), two distinct peaks with here shake-up peaks are observed, which are described as Cu $2p_{1/2}$ and Cu $2p_{3/2}$, respectively [49].

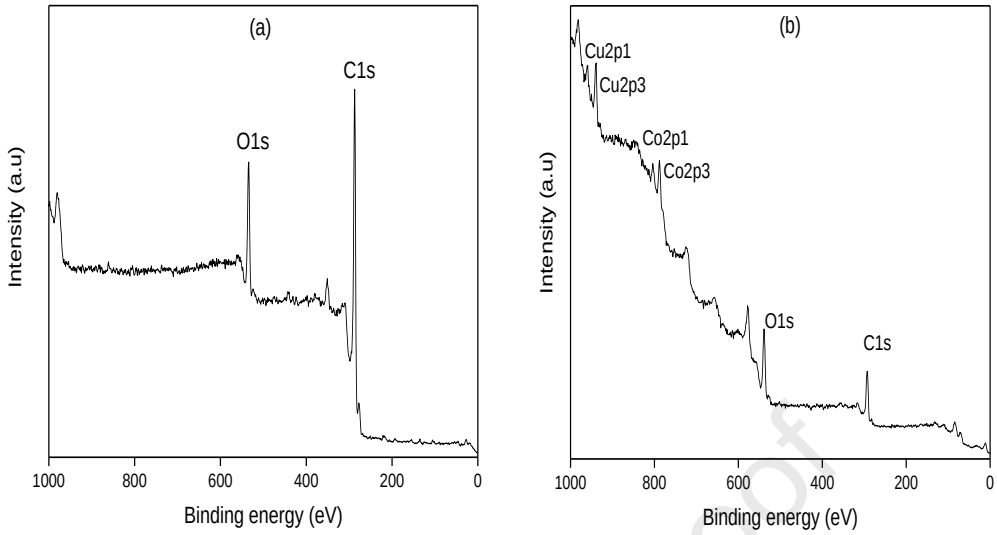

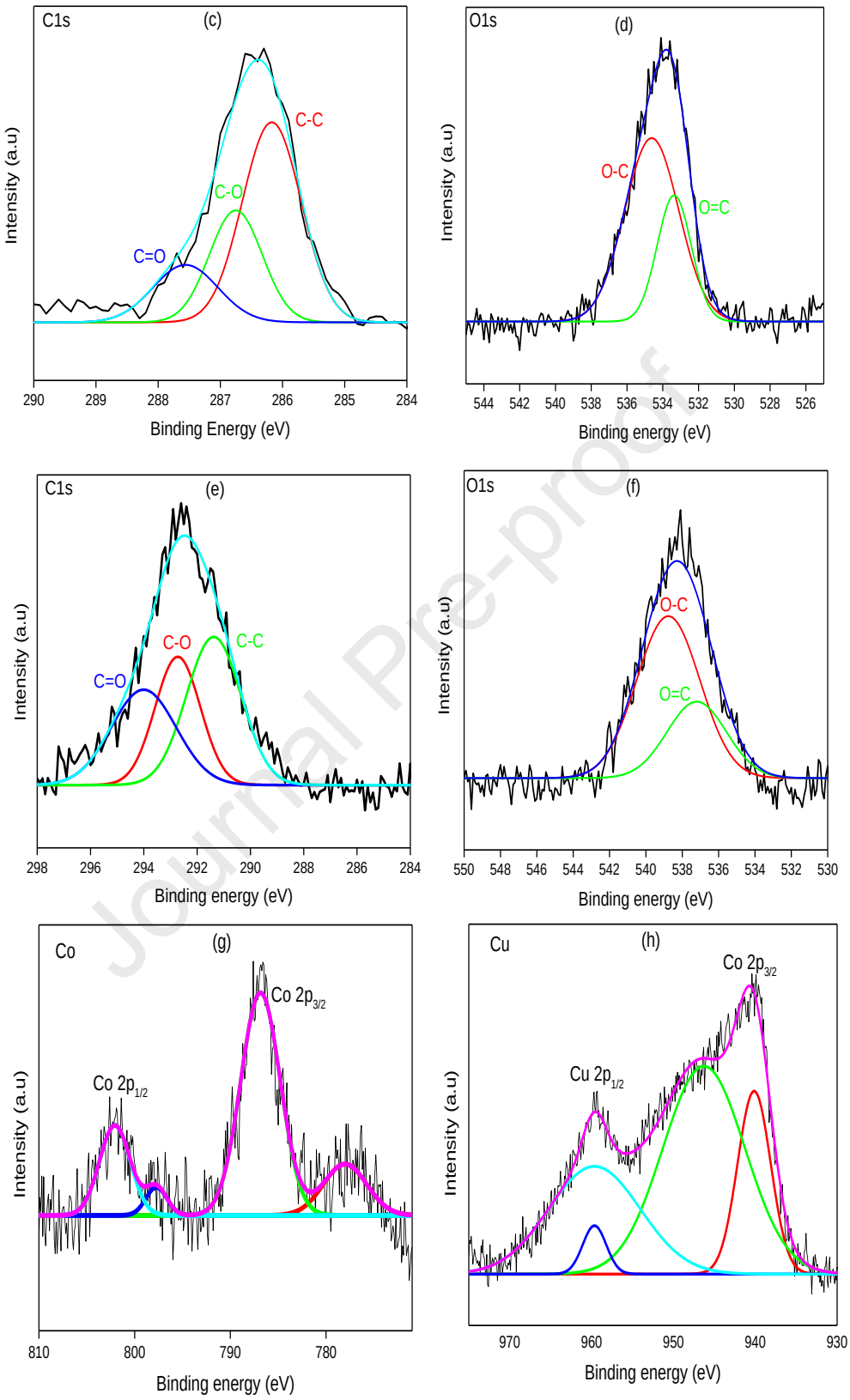

Fig. 6. XPS survey spectrum of (a) AC_{ODS} and (b) $AC_{ODS}/CuCoO_2$; Fitted XPS spectra of (c) C1s, (d) O1s, (e) Cu2p and (f) Co2p.

3.7. Raman Analysis

The Raman spectra in the range of 200-2500 cm^{-1} recorded with $CuCoO_2$ and $AC_{ODS}/CuCoO_2$ are shown in Fig. S4. Raman spectra are used to give information about oxide structure and molecular vibrations of synthesized material.

In the spectrum of $CuCoO_2$ (Fig. S4a), the peak observed at 292 cm^{-1} is assigned to E_g (O-Co-O bending) vibrational modes. The peaks localized at 473 and 518 cm^{-1} were caused by Cu vacancies or interstitial oxygen atoms defects [50]. The peak at 679 cm^{-1} may be due to the A_{1g} stretching vibration of Co-O [51]. The Raman spectrum of $AC_{ODS}/CuCoO_2$ (Fig. S4b) showed that, in addition to the oxide peaks, two bands G-band (graphite) and D-band (default) are observed around 1610 and 1353 cm^{-1}, respectively. These results due to the stretching vibration of the same carbon atoms (sp2), corresponding to E_{2g} and A_{1g} symmetries, respectively, while there are prohibited in perfect graphite [30]. By comparing the two spectra, it can be seen that the peaks of $CuCoO_2$ were shifted in the spectrum of the hybrid compound, confirming the combination of the oxide $CuCoO_2$ and activated carbon AC_{ODS} to form the hybrid material.

3.8. Thermogravimetric analysis (TGA)

TGA was employed to evaluate the change in the mass of the materials under thermal treatment. The thermograms of activated carbon AC_{ODS} and $AC_{ODS}/CuCoO_2$ are shown in Fig. S5. From these curves, it is found that the activated carbon exhibited three specific weight losses. The first stage shows a slight loss of weight, which is probably due to the desorption of residual moisture (hydrating water molecules: H_2O). The second degradation occurs around 200-300 °C may be due to the decomposition of hemicellulose [52]. The third decomposition observed around 300-600°C is attributed to the breakdown of cellulose and lignin into carboxyl, lactone and carbonyl [53]. However, the addition of $CuCoO_2$ oxide to the activated carbon improved the thermal stability of AC_{ODS} and facilitates the elimination of organic compounds. The

thermogram of $AC_{ODS}/CuCoO_2$ exhibited two specific weight losses. The first weight loss was observed below 300 °C, which can be assigned to the elimination of water molecules. The second weight loss in a range of 300−800 °C is due to the decomposition of carbonaceous materials of activated carbon. Further, no significant weight loss was observed above 800 °C, thus confirming stability of the composite.

3.9. Electrochemical performance of the prepared electrodes

3.9.1. Cyclic voltammetry

The electrochemical properties of the $AC_{ODS}/CuCoO_2$ hybrid material were studied by cyclic voltammetry. The waves observed on the voltammograms recorded in Fig. 7a due to the redox reactions of copper and cobalt in the bimetallic oxide ($CuCoO_2$) introduced into the activated carbon AC_{ODS}. Compared with the CV characteristics of pure AC_{ODS}, there is an appearance of pseudocapacitive performance after the surface modification by redox-active $CuCoO_2$ within AC_{ODS}. According to the XPS analysis and the CV recorded in acidic medium, both metals are oxidized and reduced on the activated carbon matrix following the reaction below:

$$AC_{ODS}\text{-}[Cu^{+I}Co^{+III}O_2]+2H^{+}+2e^{-} \leftrightarrow AC_{ODS}\text{-}\ H_2[Cu^{+II}Co^{+II}O_2]$$

A redox and pseudocapacitive phenomenon following the same type of reaction was observed with activated carbon and vanadium oxide [54].

The current response of the $AC_{ODS}/CuCoO_2$ electrode at different scan rates is shown in Fig. 7b. As the scan rate increases, the area of the voltammograms also increases, resulting in a high specific capacity. The oxidation and reduction waves are shifted to the anodic and cathodic values with increasing scan rate. It should be noted that the CV curves are not rectangular (lack of symmetry) because redox waves are clearly observed, suggesting ideal pseudocapacitive behavior [55, 56]. This result is due to the capacitive effect of the activated carbon and the redox reactions of the metals present in the bimetallic oxide [57].

To estimate the charge storage dynamics of the prepared electrode, the b value from the CV spectra is determined from the slope of the plot of *log (i) vs. log (v)* (Fig. 7c). Basing on this plot, the *b*-value found at lower potentials (<0.2 V) is 0.8. This value is located between 0.7 and 1, indicating the presence of two behaviors at the same time such as capacitive process (redox reactions) and EDLC [58].

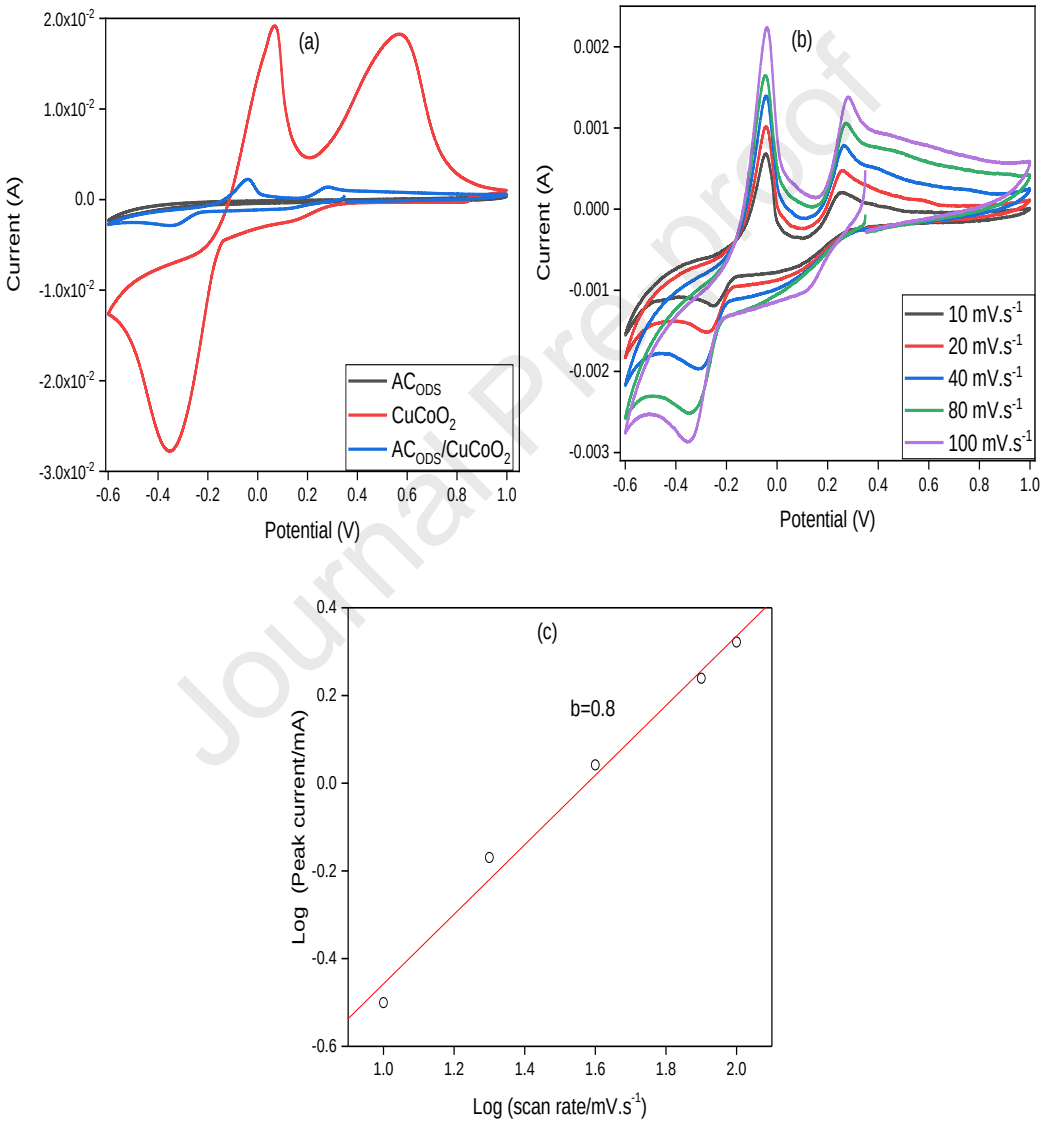

Fig. 7. Cyclic voltammograms of (a) different compounds; (b) with $AC_{ODS}/CuCoO_2$ electrode at different scan rates in three electrodes system and 1M H_2SO_4/KCl and (c) log (Peak current) vs. log (Scan rate) plot.

3.9.2. Charge-discharge capacities of the prepared electrodes

The GCD measurements are made in the 0-1V voltage range (Fig. 8). The GCD plots show no triangular demonstrate nonlinear discharge curves [59, 60], confirming that the faradic charge storage mechanism is predominant in the material [61], behavior and correlating with the CV measurements.

Figure 8a shows the galvanostatic charge-discharge behavior of the $AC_{ODS}/CuCoO_2$ working electrode using a three-electrode system for the determination of specific capacitance in the specific current range between 0.3 and 2 $A.g^{-1}$, and in the potential range from 0 to 1 V. On the other hand, Fig. 8b reports the charge-discharge behavior of the same electrode using two-electrode system for the calculation of specific energy, specific power and specific capacitance at the specific current range of 0.3-8 $A.g^{-1}$. The asymmetric curves (Figs. 8a, b) represent the characteristics of a pseudocapacitive process (Faradic current). Furthermore, as the specific current increases, the specific capacitance calculated using two-electrode system decreases as shown in Table 1. The specific capacitance and specific capacity of the $AC_{ODS}/CuCoO_2$ electrodes are 1052.95 $F.g^{-1}$ and 219.26 $mAh.g^{-1}$ at 0.3 $A.g^{-1}$, and 650.51 $F.g^{-1}$ and 111.84 $mAh.g^{-1}$ at 1 $A.g^{-1}$, respectively. The $AC_{ODS}/CuCoO_2$ electrode appears to be a promising candidate for supercapacitor development.

Fig. 8c illustrates the $AC_{ODS}/CuCoO_2$ material's cyclic stability over 10^4 cycles with a specific current of 20 $A.g^{-1}$ and a potential range of 0 to 1 V in 1M H_2SO_4/KCl. According to Fig. 8b, c, the $AC_{ODS}/CuCoO_2$ electrode can reach up to the high specific capacitance of 1052.95 $F.g^{-1}$ and possess outstanding capacitance retain ratio of 95.41% after 10^4 cycles, confirming excellent electrochemical stability of the electrode material.

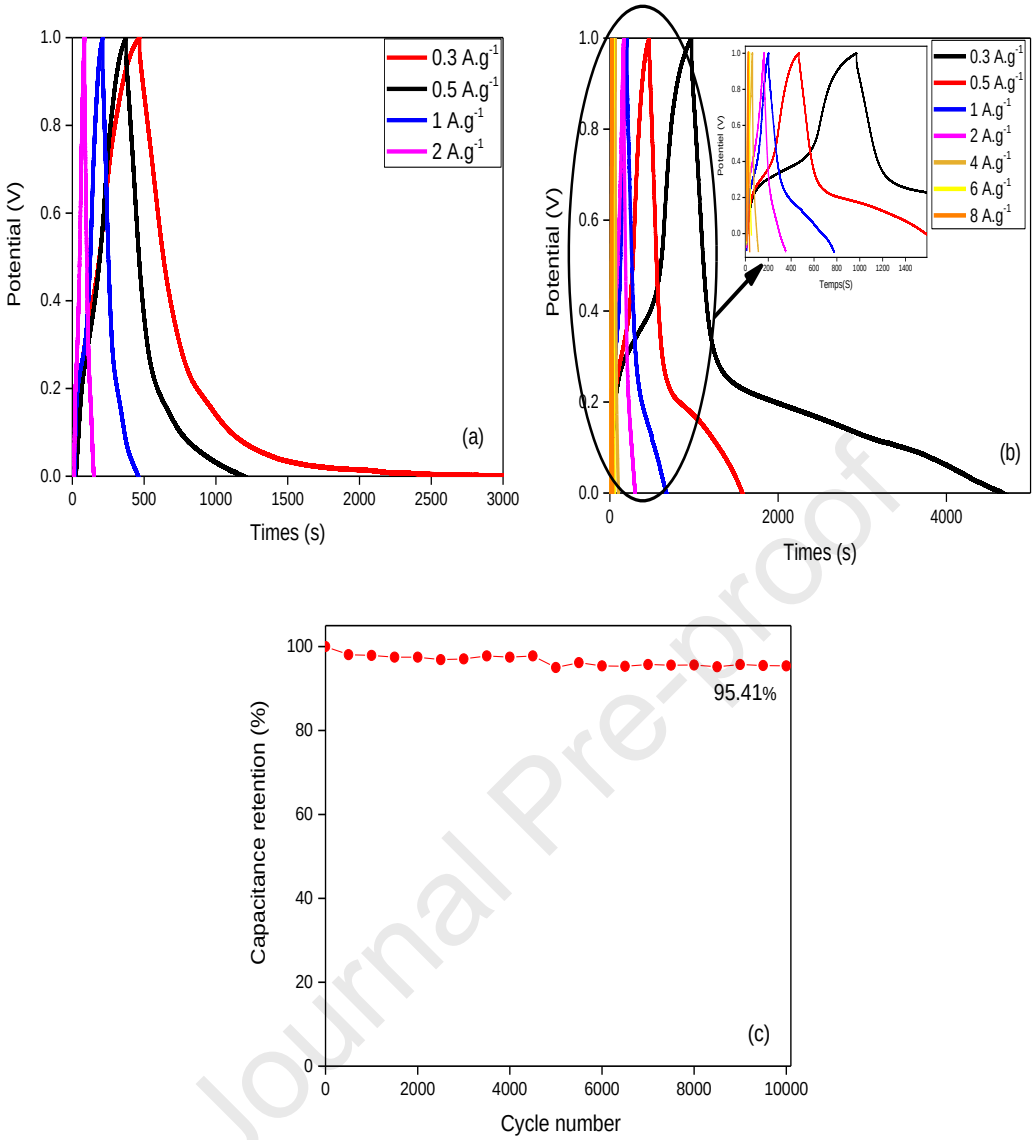

Fig. 8. Galvanostatic charge discharge curves using $AC_{ODS}/CuCoO_2$ in (a) three electrodes systems and (b) two electrodes systems with 1M (H_2SO_4/KCl) electrolyte; (c) Cyclic stability of the $AC_{ODS}/CuCoO_2$ electrode.

Table 1. The comparison of both specific energy and specific capacitance of $AC_{ODS}/CuCoO_2$ in mixture of 1M KCl-1M H_2SO_4 electrolyte.

	Specific Current ($A.g^{-1}$)	* Specific Capacity (Q_s/$mAh.g^{-1}$)	Specific Capacitance ($C/F.g^{-1}$)	Specific Energy ($E/Wh.Kg^{-1}$)	Specific power ($P/W.Kg^{-1}$)
$AC_{ODS}/CuCoO_2$	0.3	219.26	1052.95	161.23	157.5
	0.5	111.94	650.51	101.51	265.0
	1	68.33	555.71	81.88	515.0
	2	36.66	386.31	51.52	980.0
	4	-	168.26	18.92	1800.0
	6	-	126.92	9.91	2250.0
	8	-	103.12	6.05	2600.0

** The specific capacity ($mAh.g^{-1}$) was calculated using three electrodes.*

Based on Fig. 9, the specific energy and specific power of the $AC_{ODS}/CuCoO_2$ material were calculated, using a symmetrical two electrode system (Table 2).

Figure 9a shows the specific capacitance as a function of the specific current, it shows that increasing specific current causes lower specific capacitance values. However, it was found that when the specific energy increases the specific power decreases (Fig. 9b).

The specific energy and specific power are 161.23 $Wh.Kg^{-1}$ and 157.5 $W.Kg^{-1}$ for a specific current of 0.3 $A.g^{-1}$, and 6.05 $Wh.Kg^{-1}$ and 2600 $W.Kg^{-1}$ for a specific current of 8 $A.g^{-1}$, respectively.

In conclusion, the chemical composition in metals of the ternary oxide of the $AC_{ODS}/CuCoO_2$ electrode allowed to increase the specific capacitance of this one due to the presence of more free electrons that improve the electronic conductivity of the material.

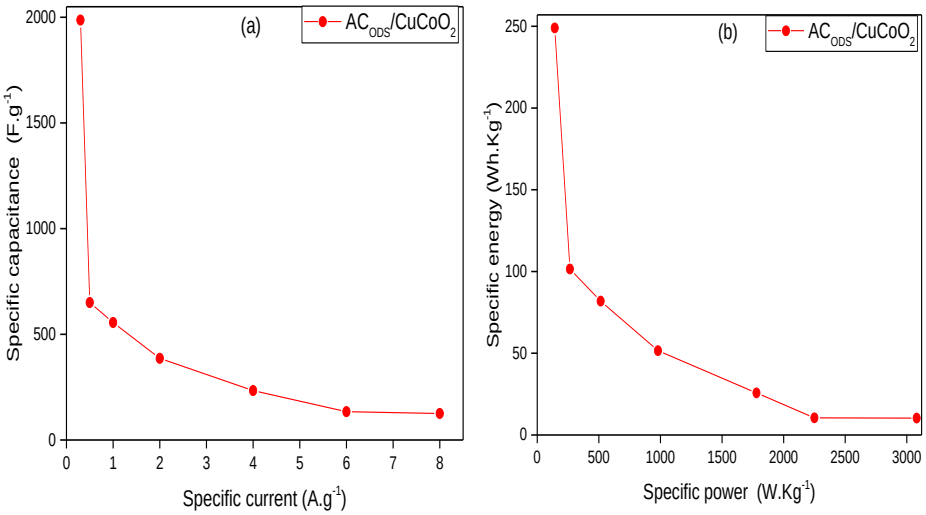

Fig. 9. (a) Specific capacitance versus specific current, (b) Specific energy versus specific power of $AC_{ODS}/CuCoO_2$.

The specific capacitance values of the $AC_{ODS}/CuCoO_2$ modified electrode as a function of specific current were compared with those calculated with other electrodes based on different metal oxides as shown in Table 2. We notice that the AC_{ODS} activated carbon combined with the ternary $CuCoO_2$ oxide gives the best results in terms of specific capacitance compared to other hybrid materials prepared with other metal oxides [31, 62-68]. This finding can be explained by the increase in the number of reaction sites with the AC_{ODS} activated carbon and the $CuCoO_2$ oxide synthesized at low temperature [69, 70]. In addition, the use of a binary electrolyte increases the conductivity and ion migration rate, which improves the electrochemical performance of the $AC_{ODS}/CuCoO_2$ electrode.

Table 2. Comparative study of the specific capacitance values of the $AC_{ODS}/CuCoO_2$ electrode material with those calculated using other metal oxide systems.

Electrode Materiels	Electrolyte	Specific Current ($A.g^{-1}$) or Scan rate	Specific Capacitance ($F.g^{-1}$)	References
$CuCoO_2$	2M KOH	0.5	250	[31]
$CuCo_2O_4$ nanosheets	6M KOH	1.0	100	[62]
CoNi–$CoNiO_2$ NPs	6 M KOH	0.25	280	[63]
MnO_2/grapheneoxide/ Polypyrrole	5M KOH	0.5	480	[64]
$NiCo_2O_4/NiMoO_4$	3 M KOH	1.0	85.6	[65]
CFAC/Ni&Co oxides	6 M KOH	1.0	222	[66]
CuO	1M Na_2SO_4	5 $mV.S^{-1}$	158	[67]
ZnO/Graphene	1 M KCL	5 $mV.S^{-1}$	109	[68]
$AC_{ODS}/CuCoO_2$	1M KCl/	0.3	1052.95	This work
	1M H_2SO_4	1.0	555.71	This work

3.9.3. Electrochemical impedance spectroscopy (EIS)

To better understand the electrochemical performance of our hybrid material, an EIS study was performed at room temperature. Fig. 10 a shows the Nyquist diagram recorded with the $AC_{ODS}/CuCoO_2$ electrode and fitted with an equivalent circuit. The latter consists of a solution resistance R_s (2.16 Ω), a very low charge transfer resistance R_{tc} (15 Ω), lower than that of activated carbon alone, a capacitance of 41.7 mF, and a Warburg impedance (W: 0.016) (AC_{ODS} [30]: R_{tc}: 19.4 Ω; W: 0.020 and C: 0.5 mF), which proves the improved conductivity of the $AC_{ODS}/CuCoO_2$ electrode [71]. The increase of the electrical conductivity with hybrid composite $AC_{ODS}/CuCoO_2$ can be explained by the addition of the metal oxide into the activated carbon surface, modifying the interfaces between $CuCoO_2$ and AC_{ODS}, resulting in a larger interface area. This promotes the penetration of electrolyte ions into the porous structure of the

composite through the expanded interfaces, resulting in an improvement in the specific capacitance and charge-discharge properties of supercapacitor electrode [72].

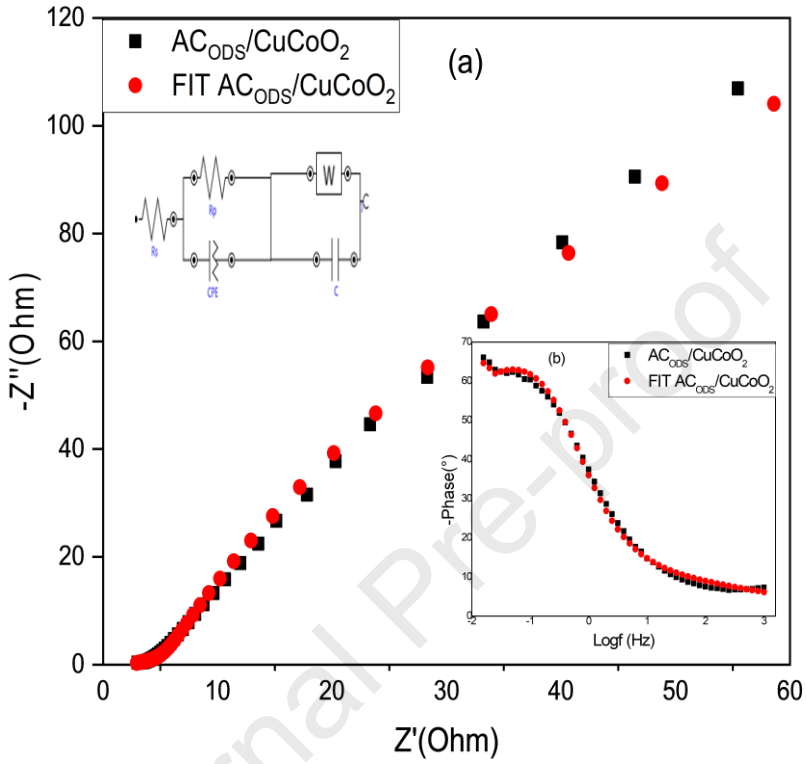

Fig. 10. (a) Nyquist diagram, (b) Bode phase angle diagram and the equivalent circuit recorded with the $AC_{ODS}/CuCoO_2$ hybrid compound.

4. Conclusion

In this work, the synthesis and characterization of the $AC_{ODS}/CuCoO_2$ hybrid compound were successfully completed. Electrochemical studies by cyclic voltammetry and galvanostatic charge-discharge revealed that activated carbon-modified with $CuCoO_2$ oxide significantly improved specific capacitance and specific energy by applying high specific current. Electrochemical results showed that the $AC_{ODS}/CuCoO_2$ electrode achieved a specific capacitance and specific capacity of 1052.9 $F.g^{-1}$ and 219.3 $mAh.g^{-1}$, respectively, in 1M H_2SO_4/KCl at a specific current of 0.3 $A.g^{-1}$. In addition, this electrode showed a high specific energy (161.2 $Wh.kg^{-1}$) at high current (8 $A.g^{-1}$).

Electrode stability of the $AC_{ODS}/CuCoO_2$ hybrid material exhibits high cycle stability with 95.41% capacitance retention after 10,000 cycles at 20 $A.g^{-1}$.

The EIS study showed that the $AC_{ODS}/CuCoO_2$ material has an extremely low charge transfer resistance R_{tc} (15 Ω) and a capacitance of 41.7 mF, which proves that the $AC_{ODS}/CuCoO_2$ electrode has good conductivity in aqueous media.

Based on these results, the $AC_{ODS}/CuCoO_2$ hybrid material can be used as supercapacitor electrodes for energy storage.

Acknowledgements

The authors would like to acknowledge the MESRS Algerian Ministry and Directorate-General for Scientific Research and Technological Development (Algeria) for supporting the present research.

Declaration of competing interest

The authors declare that they have no known competing financial interests or personal relationships that could have appeared to influence the work reported in this paper.

Data availability

Data will be made available on request.

Reference

[1] C. Fan, X. Zhang, L. Chen, H. Fu, H. Li, J. Hou, F. Yu, H. Li, Y. Shi, X. Guo, Preparation of mesoporous $CoNiO_2$ hexagonal nanoparticles for asymmetric supercapacitors via a hydrothermal microwave carbon bath process. New J. Chem. 43 (2019) 15066-15071.

[2] X. Lv, S. Ji, V. Linkov, X. Wang, H. Wang, R. Wang, Three-dimensional N-doped super-hydrophilic carbon electrodes with porosity tailored by Cu_2O template-assisted electrochemical oxidation to improve the performance of electrical double-layer capacitors. J. Mater. Chem. A 9 (2021) 2928-2936.

[3] S.T. Hameed, T.F. Qahtan, A;M. Abdelghany, A.H. Oraby, ZnO/CuO nanocomposite-based carboxymethyl cellulose/polyethylene oxide polymer electrolytes for energy storage applications. J. Mater. Res. Technol. 22 (2023) 531-540.

[4] M. Ibrahim, Z. Wen, X. Sun, H.N. Abdelhamid, In situ polymerization of a melamine-based microsphere into 3D nickel foam for supercapacitors. RSC Adv. 14(8) (2024) 5566-5576.

[5] L. Huang, D. Chen, Y. Ding, S. Feng, Z.L. Wang, M. Liu, Nickel–cobalt hydroxide nanosheets coated on $NiCo_2O_4$ nanowires grown on carbon fiber paper for high-performance pseudocapacitors. Nano lett. 13 (2013) 3135–3139.

[6] Q. Shi, W. Ren, W. Kong, L. Wang, C. Ma, C., A. Xu, J. Chang, C. Jiang, Oxidation mode on charge transfer mechanism in formation of Mn–Co–Ni–O spinel films by RF sputtering. J. Mater. Sci. Mater. Electron. 28 (2017) 13659-13664.

[7] B. You, L. Wang, L. Yao, J. Yang, Three dimensional N-doped graphene–CNT networks for supercapacitor. Chem. Comm. 49 (2013) 5019-5018.

[8] C. Guan, X. Li, Z. Wang, X. Cao, C. Soci, H. Zhang, H.J. Fan, Nanoporous walls on macroporous foam: rational design of electrodes to push areal pseudocapacitance. Adv. Mater. 24 (2012) 4186-4190.

[9] V. Shrivastav, S. Sundriyal, U.K. Tiwari, K-H. Kim, A. Deep, Metal-organic framework derived zirconium oxide/carbon composite as an improved supercapacitor electrode, Energy 235 (2023) 121351.

[10] J. Jose, S.P. Jose, T. Prasankumar, S. Shaji, S. Pillai, Emerging ternary nanocomposite of rGO draped palladium oxide/polypyrrole for high performance supercapacitors. J; Alloys Compd. 855 (2021) 157481.

[11] H.N. Abdelhamid, S.A. Al Kiey, W. Sharmoukh, A high-performance hybrid supercapacitor electrode based on ZnO/nitrogen-doped carbon nanohybrid. Appl. Organomet. Chem. 36(1) (2022) e6486.

[12] S.A. Al Kiey, H.N. Abdelhamid, Metal-organic frameworks (MOFs)-derived Co_3O_4@ N-doped carbon as an electrode materials for supercapacitor. J. Energy Storage 55 (2022) 105449.

[13] R. Manickam, J. Yesuraj, K. Biswas, Doped $CuCrO_2$: a possible material for supercapacitor applications. Mat. Sci. Semicon. Proc. 109 (2020) 104928.

[14] K.J. Kim, M. Balaish, M. Wadaguchi, L. Kong, J.L. Rupp, Solid-state Li–metal batteries: challenges and horizons of oxide and sulfide solid electrolytes and their interfaces. Adv. Energy Mater. 11 (2021) 2002689.

[15] S.Y. Zhao, B. Zhang, H. Su, J.J. Zhang, X.H. Li, K.X. Wang, P. Feng, Enhanced oxygen electroreduction over nitrogen-free carbon nanotube-supported $CuFeO_2$ nanoparticles. J. Mater. Chem. A. 6 (2018) 4331-4336.

[16] M.A. Madre, M.A. Torres, J.A. Gomez, J.C. Diez, A. Sotelo, A. Effect of alkaline earth dopant on density, mechanical, and electrical properties of Cu 0.97 AE 0.03 CrO_2 (AE= Mg, Ca, Sr, and Ba) delafossite oxide. J. Aust. Ceram. Soc. 55 (2019) 257-263.

[17] J.F.H.L. Monteiro, F.C. Monteiro, A.R. Jurelo, D.H. Mosca, Conductivity in (Ag, Mg)-doped delafossite oxide $CuCrO_2$. Ceram. Int. 44 (2018) 14101-14107.

[18] P.L. Popa, J. Crepelliere, P. Nukala, R. Leturcq, D. Lenoble, Invisible electronics: Metastable Cu-vacancies chain defects for highly conductive p-type transparent oxide. Appl. Mater. Today. 9 (2017) 9184-191.

[19] Z. Deng, B. Tong, G. Meng, H. Liu, T. Dai, L. Qi, X. Fang, Insight into the Humidity Dependent Pseudo-n-Type Response of p-$CuScO_2$ toward Ammonia. Inorg. Chem. 58 (2019) 9974-9981.

[20] Z. Du, D. Xiong, J. Qian, T. Zhang, J. Bai, D. Fang, H. Li, Investigation of the structural, optical and electrical properties of Ca^{2+} doped $CuCoO_2$ nanosheets. Dalton Trans. 48 (2019) 13753-13759.

[21] K. Rajeshwar, Hydrogen generation at irradiated oxide semiconductor–solution interfaces. J. Appl. Electrochem. 37 (2007) 765-787.

[22] D.Y. Shahriari, A. Barnabe, T.O. Mason, K.R. Poeppelmeier, A high-yield hydrothermal preparation of $CuAlO_2$. Inorg. Chem. 40 (2001) 5734-5735.

[23] C. Martin, M. Poienar, Mixed valence transition metal 2D-oxides: Comparison between delafossite and crednerite compounds. J. Cryst. Growth. 472 (2017) 71-75.

[24] J. Töpfer, M. Trari, J.P. Doumerc, Preparation and physical properties of $CuAl1-xMnxO_2$ ($0\leq x\leq 0.2$) delafossites. Solid State Sci. 9 (2007) 236-239.

[25] J. Ahmed, Y. Mao, Synthesis, characterization and electrocatalytic properties of delafossite $CuGaO_2$. Solid State Sci. 242 (2016) 77-85.

[26] S. Ramesh, A. Kathalingam, K. Karuppasamy, H.S. Kim, H.S. Kim, Nanostructured CuO/Co_2O_4@ nitrogen doped MWCNT hybrid composite electrode for high-performance supercapacitors. Composites Part B: Engineering 166 (2019) 74-85.

[27] B. Heng, C. Qing, D. Sun, B. Wang, H. Wang, Y. Tang, Rapid synthesis of CuO nanoribbons and nanoflowers from the same reaction system, and a comparison of their supercapacitor performance. RSC Adv. 3 (2013) 15719-15726.

[28] H. Gao, H., X. Liu, N. Han, L. Shi, L. Wang, Y. Mi, D. Xiong, Nanocrystals of $CuCoO_2$ derived from MOFs and their catalytic performance for the oxygen evolution reaction. Dalton Trans. 51 (2022) 11536-11546.

[29] D. Xiong, Z. Du, H. Li, J. Xu, J. Li, X. Zhao, L. Liu, Polyvinylpyrrolidone-assisted hydrothermal synthesis of $CuCoO_2$ nanoplates with enhanced oxygen evolution reaction performance. ACS Sustain. Chem. Eng. 7 (2018) 1493-1501.

[30] K. Ait Kaci Azzou, A. Terbouche, C. Ait Ramdane-Terbouche, H. Belkhalfa, K. Bachari, D. Hauchard, D. Mezaoui, Electrochemical performance of new hybrid activated carbon

materials from binary and ternary Date-Olive pits for supercapacitor electrodes. J. Energy Storage 47 (2022) 103559.

[31] M. Isacfranklin, R. Yuvakkumar, G. Ravi, M. Pannipara, A.G. Al-Sehemi, $CuCoO_2$ electrodes for supercapacitor applications. Mater. Lett. 296 (2021) 129930.

[32] R. Boopathi Raja, M. Parthibavarman, A.N. Begum, Hydrothermal induced novel $CuCo_2O_4$ electrode for high performance supercapacitor applications. Vacuum 165 (2019) 96-104.

[33] D.J. Tarimo, K.O. Oyedotun, A.A. Mirghni, N.F. Sylla, N. Manyala, High energy and excellent stability asymmetric supercapacitor derived from sulphur-reduced graphene oxide/manganese dioxide composite and activated carbon from peanut shell. Electrochim. Acta. 353 (2020) 136498.

[34] A.A. Mirghni, K.O. Oyedotun, O. Fasakin, B.A. Mahmoud, D.J. Tarimo, N. Manyala, High-performance bimetallic Ni-Mn phosphate hybridized with 3-D graphene foam for novel hybrid supercapacitors. J. Energy Storage 31 (2020) 101584.

[35] Y. Peng, W. Yuan, X. Liu, P. Xie, F. Yang, H. Zhao, Z. Wu, All-in-one integration of polyaniline-polyvinyl alcohol electrode/electrolyte interface for tailorable solid-state supercapacitors. J. Energy Storage 61 (2023) 106701.

[36] Y. Chen, H. Ren, D. Rong, Y. Huang, S. He, Q. Rong, Stretchable all-in-one supercapacitor enabled by poly (ethylene glycol)-based hydrogel electrolyte with low-temperature tolerance. Polym. 270 (2023) 12796.

[37] R. Prasad, P. Singh, Low temperature complete combustion of a lean mixture of LPG emissions over cobaltite catalysts. Catal. Sci. Technol. 3 (2013) 3223-3233.

[38] Q. Li, L. Zeng, J. Wang, D. Tang, B. Liu, G. Chen, M. Wei, Magnetic mesoporous organic−inorganic $NiCo_2O_4$ hybrid nanomaterials for electrochemical immunosensors. ACS Appl. Mater. Interfaces 3 (2011) 1366-1373.

[39] A.C. Nwanya, S. Botha, F.I. Ezema, M. Maaza, Functional metal oxides synthesized using natural extracts from waste maize materials. Curr. Res. Green Sustain. Chem. 4 (2021) 100054.

[40] B. Boukoussa, K.R. Cherdouane, R. Zegai, A. Mokhtar, M. Hachemaoui, I. Issam, I., J. Iqbal, S.P. Patole, F.Z. Zeggai, R. Hamacha, M. Abboud, Preparation of activated carbon-metal nanoparticle composite materials for the catalytic reduction of organic pollutants. Surf. Interfaces 44 (2024) 103622.

[41] M. Baikousi, A. Gantzoudi, C. Gioti, D. Moschovas, A.E. Giannakas, A. Avgeropoulos, C.E. Salmas, M.A. Karakassides, Hydrogen Sulfide Removal via Sorption Process on Activated Carbon–Metal Oxide Composites Derived from Different Biomass Sources. Molecules 28(21) (2023) 7418.

[42] M.A. Hegazy, M.M. Mohammedy, A.S. Dhmees, Phosphorous and sulfur doped asphaltene-derived activated carbon for supercapacitor application. J. Energy Storage 44 (2021) 103331.

[43] N.M. El-Shafai, M.S. Ramadan, K.M. Alkhamis, M.M. Aljohani, N.M. El-Metwaly, I.M.A. El-Mehasseb, unique engineering building of nanoelectrodes based on titanium and metal oxides nanoparticles captured on graphene oxide surface for supercapacitors and energy storage. J. Alloys Compd. 939 (2023) 168685.

[44] Z. Du, J. Qian, T. Zhang, C. Ji, J. Wu, H. Li, D. Xiong, Solvothermal synthesis of $CuCoO_2$ nanoplates using zeolitic imidazolate framework-67 (ZIF-67) as a co-derived precursor, New J. Chem. 43(38) (2019) 15233-15239.

[45] H. Gao, X. Liu, N. Han, L. Shi, L. Wang, Y. Mi, X.-Q. Bao, J. Bai, H. Li, D. Xiong, Nanocrystals of $CuCoO_2$ derived from MOFs and their catalytic performance for the oxygen evolution reaction. Dalton Trans. 51(30) (2022) 11536-11546.

[46] G. Greczynski and L. Hultman, C 1s peak of adventitious carbon aligns to the vacuum level: dire consequences for material's bonding assignment by photoelectron spectroscopy,

ChemPhysChem 18 (2017) 1507-1512.

[47] G. Greczynski, L. Hultman, Undressing the myth of apparent constant binding energy of the C 1 s peak from adventitious carbon in x-ray photoelectron spectroscopy. Sci. Talks, 1 (2022) 100007.

[48] T. Aghavnian, J.B. Moussy, D. Stanescu, R. Belkhou, N. Jedrecy, H. Magnan, P. Ohresser, M.-A. Arrio, P. Sainctavit, A. Barbier, Determination of the cation site distribution of the spinel in multiferroic $CoFe_2O_4/BaTiO_3$ layers by X-ray photoelectron spectroscopy. J. Electron Spectros. Relat. Phenomena 202 (2015)16-21.

[49] R. Li, W. Xu, X. Lu, X., Y. Fang, M. Xu, C. Luo, H. Peng, H. Lin, C. Duan, Dual Selective Gas Sensor Based on Delafossite $CuCoO_2$ with Instantaneously Attenuated Response to Amine at Room Temperature. ACS Appl. Electron. Mater. 5(11) (2023) 6324-6333.

[50] M. Isacfranklin, R. Yuvakkumar, G. Ravi, M. Pannipara, A.G. Al-Sehemi, $CuCoO_2$ electrodes for supercapacitor applications. Mat. Let. 296 (2021) 129930.

[51] Z. Du, D. Xiong, J. Qian, T. Zhang, J. Bai, D. Fang, H. Li, Investigation of the structural, optical and electrical properties of Ca^{2+} doped $CuCoO_2$ nanosheets. Dalton Trans. 48 (36) (2019) 13753–13759.

[52] E. Gonzalez-Serrano, T. Cordero, J. Rodriguez-Mirasol, L. Cotoruelo, J.J. Rodriguez, Removal of water pollutants with activated carbons prepared from H_3PO_4 activation of lignin from kraft black liquors, J. Water Res. 38 (2004) 3043–3050.

[53] F.A.A. Mohamed, A.A. Zeid, A.H. Mohamad, C. Zlotea, M. Latroche, F. Cuevas, Hydrogen storage in Pristine and d10-block metal-anchored activated carbon made from local wastes, J. Energies 8 (2015) 3578–3590.

[54] S. Maity, A.A. Vannathan, T. Kella, D. Shee, P.P. Das, S.S. Mal, Electrochemical performance of activated carbon-supported vanadomolybdates electrodes for energy conversion. Ceram. Int. 47(19) (2021) 27132-27141.

[55] A.L.M. Reddy, M.M. Shaijumon, S.R. Gowda, P.M. Ajayan, Multisegmented Au-MnO2/carbon nanotube hybrid coaxial arrays for high-power supercapacitor applications. J. Phys. Chem. C. 114(1) (2010) 658-663.

[56] Y. Jiang, J. Liu, Definitions of pseudocapacitive materials: a brief review. Energy Environ. Mater. 2(1) (2019) 30-37.

[57] Q. Kangwen, L. Min, L. Yongsong, D. Xiwen, Engineering hierarchical nanotrees with $CuCo_2O_4$ trunks and NiO branches for high-performance supercapacitors, J. Mater. Chem. A. 5 (2017) 5820–5828.

[58] R. Kumar, M. Bag, Quantifying capacitive and diffusion-controlled charge storage from 3D bulk to 2D layered halide perovskite-based porous electrodes for efficient supercapacitor applications. J. Phys. Chem. C. 125(31) (2021) 16946–16954.

[59] A. Stott, M.O. Tas, E.Y. Matsubara, M.G. Masteghin, J.M. Rosolen, R.A. Sporea, S.R.P. Silva, Exceptional rate capability from carbon-encapsulated polyaniline supercapacitor electrodes. Energy Environ. Mater. 3(3) (2020) 389-397.

[60] Y. Zhu, P. Lu, F. Li, Y. Ding, Y. Chen, Metal-rich porous copper cobalt phosphide nanoplates as a high-rate and stable battery-type cathode material for battery–supercapacitor hybrid devices. ACS Appl. Energy Mater. 4(4) (2021) 3962-3974.

[61] M. Karthik, M., Parthibavarman, A. Kumaresan, S. Prabhakaran, V. Hariharan, R. Poonguzhali, S. Sathishkumar, One-step microwave synthesis of pure and Mn doped WO_3 nanoparticles and its structural, optical and electrochemical properties, J. Mater. Sci. Mater. Electron. 28 (2017) 6635–6642.

[62] K.K. Naik, S. Sahoo, C.S. Rout, Facile electrochemical growth of spinel copper cobaltite nanosheets for non-enzymatic glucose sensing and supercapacitor applications. Micropor. Mesopor. Mat. 244 (2017) 226-234.

[63] Y. Jiang, Y. Wang, D. Zeng, Y. Xiao, H. Wang, X. Zhang, X. Dai, Synthesis of bimetallic CoNi-$CoNiO_2$ nanoparticles embedded into mesoporous carbon as high-performance catalysts for supercapacitor electrode. Micropor. Mesopor. Mat. 272 (2018) 222-231.

[64] S. Ramesh, H.M. Yadav, K. Karuppasamy, D. Vikraman, H.S. Kim, J.H. Kim, H.S. Kim, Fabrication of manganese oxide@ nitrogen doped graphene oxide/polypyrrole (MnO_2@ NGO/PPy) hybrid composite electrodes for energy storage devices. J. Mater. Res. Technol. 8 (2019) 4227-4238.

[65] D. Cui, R. Zhao, J. Dai, J. Xiang, F. Wu, A hybrid $NiCo_2O_4$@ $NiMoO_4$ structure for overall water splitting and excellent hybrid energy storage. Dalton Trans. 28 (2020) 9668-9679.

[66] B. Abdolahi, M.B. Gholivand, M. Shamsipur, M. Amiri, Engineering of nickel-cobalt oxide nanostructures based on biomass material for high performance supercapacitor and catalytic water splitting. Int. J. Energy Res. 45 (2012) 12879-12897.

[67] A. Pendashteh, M.S. Rahmanifar, M.F. Mousavi, Morphologically controlled preparation of CuO nanostructures under ultrasound irradiation and their evaluation as pseudocapacitor materials. Ultrason. Sonochem. 21 (2014) 643-652.

[68] A. Ramadoss, S.J. Kim, Facile preparation and electrochemical characterization of graphene/ZnO nanocomposite for supercapacitor applications. Mater. Chem. Phys. 140 (2013) 405-411.

[69] V. Ganesh, S. Pitchumani, V. Lakshminarayanan, New symmetric and asymmetric supercapacitors based on high surface area porous nickel and activated carbon. J. Power Sources. 158(2) (2006) 1523-1532.

[70] R. Wang, X. Li, Z. Nie, Y. Zhao, H. Wang, Metal/metal oxide nanoparticles-composited porous carbon for high-performance supercapacitors. J. Energy Storage, 38 (2021) 102479.

[71] M. Lan, B. Liu, B., R. Zhao, M. Dong, X. Wang, L. Fang, L. Wang, Dandelion-like $CuCo_2O_4$ arrays on Ni foam as advanced positive electrode material for high-performance hybrid supercapacitors. J. Colloid Interface Sci. 566 (2020) 79-89.

[72] Q. Li, J. Cheng, B. Wang, L. Zhang, Activated carbon modified by CNTs/Ni-Co oxide as hybrid electrode materials for high performance supercapacitors. IEEE Trans. Nanotechnol. 13(3) (2014) 557-562.

List of tables

List of figures

Fig. 7. Cyclic voltammograms of (a) different compounds; (b) with $AC_{ODS}/CuCoO_2$ electrode at different scan rates in three electrodes system and 1M H_2SO_4/KCl and (c) log (Peak current) vs. log (Scan rate) plot.

Fig. 8. Galvanostatic charge discharge curves using $AC_{ODS}/CuCoO_2$ in (a) three electrodes systems and (b) two electrodes systems with 1M (H_2SO_4/KCl) electrolyte; (c) Cyclic stability of the $AC_{ODS}/CuCoO_2$ electrode.

Fig. 9. (a) Specific capacitance versus specific current, (b) Specific energy versus specific power of $AC_{ODS}/CuCoO_2$.

Fig. 10. (a) Nyquist diagram, (b) Bode phase angle diagram and the equivalent circuit recorded with the $AC_{ODS}/CuCoO_2$ hybrid compound.

Fig. S1. SEM micrographs of $CuCoO_2$ oxide (1µm and 100 nm).

Fig. S2. SEM-EDX spectra of $CuCoO_2$.

Fig. S3. SEM-EDX cartography of the $CuCoO_2$ oxide.

Fig. S4. Raman spectra of (a) $CuCoO_2$ and (b) $AC_{ODS}/CuCoO_2$ compounds.

Fig. S5. Thermogravimetric analysis (TGA) of AC_{ODS} and $AC_{ODS}/CuCoO_2$ compounds.

Highlights

-Hybrid material based on ternary Date-Olive-Sugar pits (AC_{ODS}) and $CuCoO_2$ are used to prepare electrodes for supercapacitors.

-The new hybrid material (AC_{ODS}-$CuCoO_2$) was characterized by ATR, SEM, XRD, Raman, XPS, TGA and electrochemical methods.

-The AC_{ODS}-$CuCoO_2$ electrode exhibited high specific capacitance (1052.95 $F.g^{-1}$) and high specific energy (161.23 $Wh.kg^{-1}$).

-The electrode showed high cycle stability with 95.41% capacitance retention after 10000 charge-discharge cycles.

Declaration of interests

☒The authors declare that they have no known competing financial interests or personal relationships that could have appeared to influence the work reported in this paper.

☐The authors declare the following financial interests/personal relationships which may be considered as potential competing interests: